ACS APPLIED MATERIALS & INTERFACES

www.acsami.org

Research Article

Sequential Deposition of Integrated Cathode−Inorganic Separator−Anode Multilayers for High Performance Li-Ion Batteries

Jack D. Evans,* Yige Sun,* and Patrick S. Grant*

Cite This: *ACS Appl. Mater. Interfaces* 2022, 14, 34538−34551

Read Online

ACCESS | Metrics & More | Article Recommendations

ABSTRACT: A porous, spray-deposited Al_2O_3-based separator was developed to enable the direct deposition of an electrode/separator/electrode Li-ion battery full cell assembly in a single operation. The optimized sprayed separator consisted of 50 nm Al_2O_3 particles, 1 wt % poly(acrylic acid), and 5 wt % styrene−butadiene rubber, deposited from an 80:20 vol % suspension of water and isopropanol. Separators between 5 and 22 μm thick had consistent and similar porosity of ∼58%, excellent wettability, thermal stability to at least 180 °C, adequate electrochemical stability and high effective ionic conductivity of ∼1 mS cm^{-1} at room temperature in an EC/DMC electrolyte, roughly double that of a conventional polypropylene separator. A sequentially deposited three-layer $LiFePO_4/Al_2O_3/Li_4Ti_5O_{12}$ full cell, the first of its kind, showed similar rate performance to an identical cell with a conventional polypropylene separator, with a capacity of ∼50 mAh g^{-1} at 30 C. However, after cycling at 2 C for 400 cycles, Al_2O_3 separator full cells retained 96.3% capacity, significantly more than conventional full cells with a capacity of 79.2% remaining.

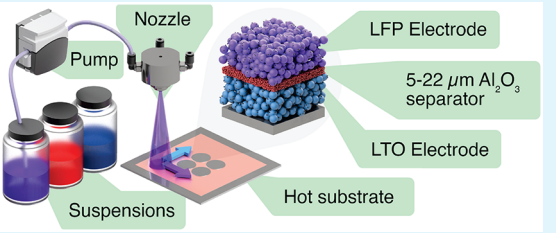

KEYWORDS: *lithium-ion battery, spray processing, inorganic separator, direct deposition, layer-by-layer full cell*

1. INTRODUCTION

A Li-ion battery (LIB) is composed of current collectors (usually Al and Cu), electrodes (anode and cathode, consisting of active material, conductive additive, and binder), an electrolyte (a lithium salt in an organic solvent mixture), and a porous separator. The separator is a membrane designed to stop electronic contact between the anode and cathode while providing pathways for lithium ion transport, and this is conventionally achieved by using an porous electronic insulator, in which the pores become filled with the Li-ion conducting electrolyte.[1] Therefore, it is favorable for these separators to have low electronic conductivity (to avoid anode−cathode short circuits), high affinity to electrolyte solvents, and high thermal, mechanical, and chemical stability and have a thickness that seeks to minimize lithium ion transport distance (typically 12−40 μm for commercial use).[1,2]

Most commercial LIB separators consist of microporous semicrystalline polyolefins, commonly polyethylene (PE), polypropylene (PP), or combinations of both (i.e., bilayer and trilayer).[3−5] Commercial PE and PP separators are manufactured by using an extrusion process, either dry (e.g., Celgard) or wet.[3,6] The dry process relies on forming pores between semicrystalline lamellar and amorphous regions in a polymer film by stretching, while the wet process relies on stretching before or after the removal of additives (which form pores on their removal).[3,6] For the dry process, the shape of the pores is characteristic to the technique, that is, slit-shaped pores, while the distribution and size of pores can be controlled by processing conditions.[3] Polyolefin separators have been favored due to low cost, a mature manufacturing process, good electrochemical stability, acceptable mechanical strength, and an intrinsic "thermal shutdown" capability.[7] However, with the desire for higher performance and safety in LIBs, improvements to their relatively poor thermal stability (shrinkage at 90 °C) and still often poor wettability are a pressing requirement.[8,9]

Researchers have focused on two methods to produce separators with higher performance: (a) modification of existing polyolefins and (b) identification and application of alternative materials and manufacturing techniques.[4] Surface coating, grafting, and blending of conventional polyolefin separators to improve wetting, thermal, mechanical, and chemical characteristics have been effective for many polymers,[10−13] ceramics/inorganics,[14−17] and combinations thereof.[18−21] However, the improvements imparted by these modifications are often coupled with a complicated manufacturing process, increased separator thickness, a decrease in porosity, and/or debonding of modifying materials during cell assembly and cycling.[1,22,23] Lee et al. provide an overview of the various modification techniques.[1]

Received: March 2, 2022
Accepted: July 9, 2022
Published: July 22, 2022

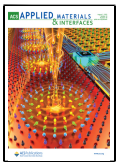

Because of the issues and compromises associated with polyolefin modification, there have been efforts to identify alternative polymeric separators. High performance polymers, such as polyimide (PI),[24,25] poly(ether ether ketone) (PEEK),[26] polytetrafluoroethylene (PTFE),[27] and poly(phenylene sulfide) (PPS)[28] offer higher mechanical strength, good chemical and electrochemical resistance, and superior thermal resistance. Liu et al. showed that an electrospun polyimide/poly(vinylidene fluoride-*co*-hexafluoropropylene) (PI/PVDF-HFP) core/sheath separator could provide higher tensile strength (53 MPa), improved dimensional stability at 150 °C, and improved electrochemical performance over a Celgard PP separator.[29] However, manufacture of separators based on higher performance polymers can be challenging due to their poor solubility in common solvents. Liu et al. recently showed that the thermally induced phase separation (TIPS) technique could overcome this challenge by preparing a thin (~30 μm) PPS separator with high porosity (~70%), excellent mechanical strength (~120 MPa tensile strength and ~7.5 GPa Young's modulus), high thermal stability (>200 °C), and improved electrochemical performance in LFP half-cells over conventional PE.[28]

Ceramic and inorganic separators have also received attention due to their high wettability, excellent thermal stability, and comparatively high stiffness (to resist deformation).[7,14,30] Common drawbacks include, in particular, the difficulty in creating a mechanically stable, thin, free-standing membrane and the often comparatively high material density (increasing the inactive mass in the cell).[31,32] Takemura et al. presented the first example of a free-standing ceramic-based separator,[33] where Al_2O_3 particles of 0.01 and 0.3 μm were combined with PVDF in varying ratios. The thermal shrinkage of the resulting separator was negligible up to 150 °C and decreased with reducing particle size and a higher powder-to-binder ratio. Cells based on an optimized oxide separator had similar capacity retention to cells using Celgard separators over 500 cycles.[33] Zhang et al. produced a free-standing 37 μm Al_2O_3 separator from 100 to 300 nm particles, 6 wt % styrene–butadiene rubber (SBR), and 1 wt % poly(ethylene glycol) (PEG)[34] and an aqueous process. On its own, SBR binder was unable to stabilize a free-standing film, while a combination of 1 wt % PEG and 6 wt % SBR produced a mechanically stable membrane. A subsequent heat treatment at 55 °C to remove the PEG resulted in dimensional stability at 130 °C for 40 min, an ~0° contact angle with the electrolyte, and improved rate performance in Li-$Ni_{1/3}Co_{1/3}Mn_{1/3}O_2$/graphite full cells when compared with conventional PE.[34]

Most ceramic/inorganic particle separators are formed by using a slurry deposition method, so direct deposition onto the electrode is an obvious route to remove processing steps in the manufacture of LIBs. For example, Lagadec et al. stated, "With time, we expect separators to be viewed as a continuation of the electrodes themselves (perhaps even directly coated on them) with both structural and chemical functionality in mind."[35] Friesen et al. described how commercial LIB cells can make use of a 2–10 μm thick coating of 500 nm Al_2O_3 particles directly deposited onto LIB anodes in combination with a polymer separator, as an alternative to coating the polymer separator directly.[36] Jung et al. directly coated 1–5 μm $Li_7La_3Zr_2O_{12}$ (LLZO) particles with 10–20 wt % PVDF-HFP directly onto graphite-based electrodes.[37] A free-standing membrane of the same type had a thickness of 30 μm, a porosity of ~40%, and no dimensional change after 1 h at 150 °C. Although the separator displayed a relatively poor electrolyte uptake of ~20%, the rate and cycle performance were improved over cells using PP separators. Significantly, the LLZO separator suppressed thermal runaway in a pouch cell during nail penetration tests, while the PP separator cell surged to ~280 °C. The thermal and dimensional stability of ceramic particles stopped direct contact between the anode and cathode, suggesting that in some cases and in comparison to conventional separators ceramic particle separators may improve cell safety.[37] Other examples of direct deposition have shown similar improvements to thermal performance but generally produced membranes between 40 and 200 μm thick, which increases the inactive cell volume and mass considerably.[38–40]

Taking direct deposition further, Singh et al. showed that a layer-by-layer spray deposition technique enabled the fabrication of a functioning full cell including the current collectors, anode, cathode, and the separator.[41] The separator consisted of PVDF, poly(methyl methacrylate) (PMMA), and fumed SiO_2 at a ratio by weight of 27:9:4, deposited from a mixture of acetone and *N*,*N*-dimethylformamide (DMF), while the rest of the components were deposited from *N*-methyl-2-pyrrolidone (NMP). A separator thickness of 200 μm was said to be necessary to prevent internal shorting due to solvent penetration during deposition of the second electrode onto the separator. Despite the relatively thick separator, the cells showed good performance in an $Li_4Ti_5O_{12}$–$LiCoO_2$ (LTO–LCO) full cell for 65 cycles and could power LEDs after being printed onto the side of a mug.[41]

The work described here advances previous examples of direct deposition of separators by providing a simple, potentially "greener" spray deposition route, paired with spray-deposited cathodes and anodes, for the sequential layer-by-layer processing of full cell assemblies. While inorganic layers have been used in combination with polymeric separators to improve thermal runaway and safety characteristics, an inorganic separator formed as an integral part of the manufacture of the full cell assembly has not been reported previously. The principal objective was to assess the promise of thin (5–22 μm) spray-deposited oxide layers in a simple electrode–separator–electrode integrated manufacturing sequence, as shown in Figure 1, which could enable the continuous sequential spray processing of LIBs. The spray-deposited separators were optimized in terms of dispersant/binder and suspension solvent, and room for further optimization remains. The proof-of-concept separators were tested with $LiFePO_4$ (LFP) positive electrodes to assess their ability to enable stable cycling of

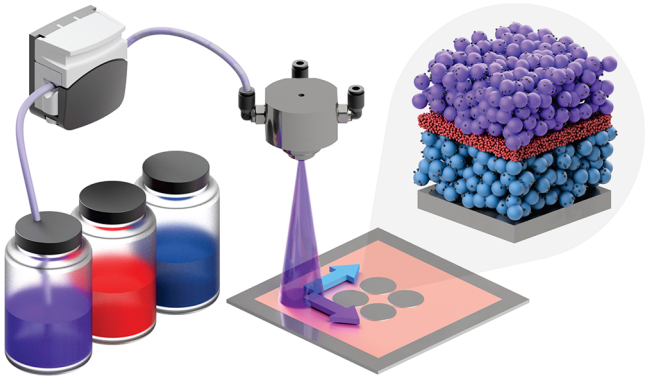

Figure 1. Schematic of the spray-printing process and the resulting microstructure of the sequential deposition of three different particle suspensions onto a stainless steel spacer to form a LIB cell.

https://doi.org/10.1021/acsami.2c03828
ACS Appl. Mater. Interfaces 2022, 14, 34538–34551

positive electrode-based half-cells. The separator that yielded the best performance was then characterized further and compared with the performance of a commercial Celgard separator in LTO-based negative electrode half-cells for oxide separators of various areal densities. Spray-deposited full cells with a thin oxide separator layer were deposited via a continuous sequential procedure, which at the time of writing is the first report of this type, as similar prior work has instead relied on direct deposition of much thicker separators.[41] We show that this arrangement provides improved wetting, thermal, rate, and degradation characteristics compared with a conventional Celgard 2500 polypropylene separator. Full experimental details are given in section 2.

2. MATERIALS AND METHODS

2.1. Electrode Suspension Preparation. $LiFePO_4$ (~100 nm primary particle size, Hydro-Quebec, Canada) was used as cathode active material and $Li_4Ti_5O_{12}$ (LTO; <200 nm, Sigma-Aldrich, UK) as the anode active material. Carbon black (C-ENERGY Super C65, Timcal Ltd., Switzerland) was used as a conductive additive, and sodium carboxymethylcellulose salt (CMC; M_w = 250000, degree of substitution 1.2, Sigma-Aldrich, UK) was used as the dispersant and binder. LFP and LTO suspensions had component ratios of 85:5:10 and 90:5:5 of active material:CMC:carbon black by mass, respectively. LFP and LTO slurries were mixed according to the following method: (1) carbon black and CMC solution were mixed by ball-milling for 15 min at 350 rpm by using 10 mm diameter ZrO_2 balls, (2) active material and water were added until a slurry concentration of 40 wt % solid was reached and then mixed for a further 15 min at 350 rpm, (3) a portion of the slurry was extracted and diluted with water to a solid concentration of 1 g/dL, (4) the suspension was agitated via magnetic stirrer, and (5) 1 min before spray deposition, the solution was diluted with IPA to a solid concentration of 0.8 g/dL and solvent ratio of 80:20 vol % water:IPA.

2.2. Separator Suspension Preparation. Spray-deposited separators consisted of <50 nm Al_2O_3 (Sigma-Aldrich, UK), poly(acrylic acid) (PAA; M_v = 1250000, Sigma-Aldrich, UK), and styrene−butadiene rubber (SBR; MTI Corp. USA) as the oxide particles, dispersant, and binder, respectively. Suspensions with a oxide:dispersant:binder ratio of 94:1:5 were prepared as follows: (1) Al_2O_3, predissolved dispersant, and deionized water were added into a ball mill and milled for 10 min at 350 rpm with 10 mm diameter ZrO_2 balls; (2) SBR solution was added, and the mixture ball-milled for a further 10 min at 350 rpm; (3) a slurry equal to 0.4 g of the solid component was diluted with water to a total volume of 80 mL and mixed for 1 min via magnetic stirring; (4) the diluted solution was sonicated for 5 min; and (5) the suspension was magnetically stirred and diluted with 20 mL of IPA to a final volume of 100 mL and a solvent ratio of 80:20 vol % water:IPA, 1 min before the spray deposition process.

2.3. Separator Suspension Characterization. Particle size and zeta-potential measurements of the suspended oxide particles were characterized by using dynamic and electrophoretic light scattering (DLS; Zetasizer, Malvern Instruments). For zeta-potential measurements, suspensions were prepared as above until step 4, at which point they were diluted with an aqueous solution of NaCl to reach an oxide particle concentration of 0.1 g/dL and 10 mM NaCl. For size measurement, the suspensions were diluted with deionized water only to 0.1 g/dL. Diluted suspensions were stirred by magnetic stirrer for 30 min before measurement.

2.4. Electrode and Separator Deposition. Electrode and separator layers were fabricated by using a spray-printing technique developed in our group, which has been described in detail previously[42−47] and shown schematically in Figure 1. Briefly, an 80 mm × 80 mm Cu foil was attached to a heated vacuum chuck by polyimide tape, and ~0.5 mm thick stainless steel spacers were placed on top. The temperature was set to 140 °C for deposition of electrodes or 150 °C for separator layers. The suspensions were fed through tubing by a Venturi pump at ~3 mL min^{-1} and atomized in an industrial spray nozzle using compressed air at 0.3 bar. During atomization, the nozzle followed a preprogrammed zigzag (snake raster) pattern in the $x-y$ plane over the spacers at a constant distance of 15 cm. As suspension droplets deposited on the hot spacers, the water and IPA components evaporated almost instantly to avoid resuspension of previously deposited material. Electrode material was deposited until an areal density of 2 and 2.3 mg cm^{-2} was achieved for LTO and LFP, respectively. All the data reported here are for uncalendered electrodes and layers, and the potential benefits or otherwise of calendering at various stages are discussed later.

For separator characterization, the separator was deposited from suspension directly onto spacers and Al foil. For half-cells, the separator was spray-deposited onto a preformed LTO electrode layer from suspension to coat the anode with a thickness of 5−22 μm. Full cells were formed by using the same process as that for half-cells up until the separator was deposited. Following this step, 3D-printed polymer masks were placed around the electrode−separator-coated spacers (to prevent connection of the second electrode with the cell casing around the cell perimeter), and the counter (LFP-based) electrode was then deposited. Full cell anode and cathode capacity was ensured to be a 1:1 ratio by measuring the spacers after deposition of each electrode and separator layer.

2.5. Electrode and Separator Physical Characterization. The mass and thickness of spacers and electrode/separator layers were measured by using an analytical balance with a readability of 0.1 mg (Sartorius Entris, Germany) and a micrometer with an accuracy of ±1 μm and a resolution of 1 μm (Mitutoyo 293 Series, Japan). Electrode surface morphology was characterized by scanning electrode microscopy (SEM; JEOL 6500F, Japan). Cross sections were prepared by using a plasma focused ion beam system (PFIB; FEI HELIOS, USA), and cross-sectional analysis was performed by using the built-in SEM and energy-dispersive X-ray spectroscopy (EDX) detectors and associated software.

The porosity was characterized by using nitrogen gas surface adsorption. Oxide separators deposited onto foil of ~25 cm^2 were evacuated and held under vacuum for 10 h in a surface area analyzer (Micromeritics Gemini V, USA). The sample was then immersed in liquid nitrogen and dosed aliquots of nitrogen for 37 steps of increasing pressure and then 30 steps of decreasing pressure. After each aliquot, pressure was equalized and the measurement performed. Manufacturer supplied software was used to model the resulting data to provide an estimation of surface area and pore width distribution.

Thermal properties of separators and their constituent components were characterized by thermogravimetric analysis (TGA; PerkinElmer Pyris, USA) in nitrogen gas from 25 to 900 °C at a 10 °C min^{-1} heating rate. For each sample, the TGA dish was coated with a bed of inert oxide powder to protect the Pt crucible from contamination. The Celgard 2500 separator was cut to the size of the dish, spray-deposited separators were scraped off the substrate, and powder samples were tested as-supplied. The mass loading of samples, dependent on the sample volume, was an average of ~4 mg.

2.6. Cell Assembly. Cells were assembled according to the type of separator, the cell type, and the characterization techniques required, including separator-only cells, half-cells, and full cells for both conventional Celgard and spray-deposited separators. Separator-only cells (i.e., no anode or cathode) were assembled for linear sweep voltammetry and impedance testing. Unless stated otherwise, components were supplied by MTI Corp. USA.

Spray-deposited electrodes, Al_2O_3 separators, and combinations thereof were dried in a vacuum for 12 h at 150 °C in a vacuum oven (MTI Corp.) within a glovebox with an Ar atmosphere of <0.1 ppm of H_2O and <0.1 ppm of O_2. Half-cells, using Celgard 2500 separators as an example, were assembled with the following components placed one after another in the center of a stainless steel CR2032 coin cell cup: (1) a stainless steel spacer coated with working electrode (0.5 mm thick, 15.5 mm diameter), (2) 75 μL of $LiPF_6$ EC/DMC = 50/50 (v/v) electrolyte (Sigma-Aldrich), (3) a Celgard 2500 separator (0.025 mm thick, 19 mm diameter), (4) 75 μL of $LiPF_6$ EC/DMC = 50/50 (v/v) electrolyte, (5) Li foil (0.6 mm thick, 16 mm), (6) a stainless steel spacer (0.5 mm thick, 15.5 mm diameter), (7) a stainless steel wave

https://doi.org/10.1021/acsami.2c03828
ACS Appl. Mater. Interfaces 2022, 14, 34538−34551

spring (0.3 mm height), and (8) a stainless steel CR2032 coin cell cap. For Celgard full cells, the Li foil, i.e., component 5, was replaced with a spacer coated with a spray-deposited counter electrode. For linear sweep voltammetry, a spacer replaced the spray-deposited electrode, i.e., component 1. For impedance testing, both electrodes, i.e., components 1 and 5, were replaced with spacers.

For spray-deposited separator half-cells, 150 μL of electrolyte was dispensed on top of an electrode−separator-coated spacer and assembled from step 5. For three-layer spray-deposited full cells, a spacer coated with a working electrode, separator layer, and counter electrode was placed in the coin cell cup, 150 μL of electrolyte was dispensed on top, and assembly continued from step 6. For linear sweep voltammetry, a spacer coated with a separator layer was placed in the coin cell cup, 150 μL of electrolyte was dispensed on top, and assembly continued from step 5. For impedance testing, a spacer coated with a separator layer was placed in the coin cell cup, 150 μL of electrolyte was dispensed into the cell, a spacer was placed on top, and assembly was continued from step 6.

The assembled cells were crimped by using a coin cell crimper (MTI MSK-160E Electric Crimper, USA) and cleaned with ethanol after removal from the glovebox. Cells were allowed to rest for at least 20 h before initial cycling was performed.

2.7. Electrochemical Characterization. Electrochemical characterization was performed by using electrochemical impedance spectroscopy (EIS; Gamry Instruments Reference 600, USA), linear sweep voltammetry (Gamry Instruments Reference 600, USA), and galvanostatic cycling (Arbin Instruments BT-G-25 and IBT21084LC, USA).

The separator-only cell EIS response was measured between 200 kHz and 1 Hz at open circuit voltage, 20 h after construction. Fitting of separator EIS data was performed according to an R-CPE equivalent circuit, where R is a resistor in series with a constant phase element (CPE). The effective resistance of the electrolyte through the separator was estimated from the intersection of a best fit of the Nyquist plot with the real impedance axis. The effective ionic conductivity of the separator was calculated from the effective resistance and physical measurements of the separator according to

$$\sigma = \frac{d}{R_0 A} \quad (1)$$

where σ is the effective ionic conductivity, d is the separator thickness, R_0 is the effective resistance of the electrolyte, and A is the separator area.

Linear sweep voltammetry measurements were collected on a potentiostat/galvanostat/ZRA system (Gamry Instruments Reference 600, USA). After resting for 20 h, spacer/separator/Li cells were subjected to a linear voltage sweep between 2 and 6 V vs Li/Li^+ at a rate of 1 mV s^{-1}.

LTO−Li coin cells were galvanostatically charged and discharged for three cycles at each rate between 0.1 and 1 C and cycled five times at each rate between 2 and 30 C before one cycle at 0.1 C. Long-term cycling was performed at 2 C for 400 cycles after rate cycling. Full cells of LTO−LFP were galvanostatically charged and discharged between 1 and 2.5 V, with two extra cycles at 0.1 C after rate cycling and seven cycles at 2 C to reach a steady state before long-term cycling. Capacity loss per cycle during long-term cycling was calculated by using linear regression for both half-cells and full cells.

3. RESULTS AND DISCUSSION

3.1. Suspension, Substrate, and Deposition Optimization. To achieve a functional spray-deposited oxide separator, i.e., controllable and reproducible thickness, acceptable roughness, balanced density/porosity, and short resistant, an initial optimization was performed for the separator suspension, substrate choice, and deposition parameters.

Dispersant Selection. Table 1 shows the dispersion characteristics of the 50 nm Al_2O_3 particles used in the sprayed separators in water as a function of several common aqueous thickeners and pH modifiers. With no dispersant, the Al_2O_3 particles had a zeta-potential of 15.9 mV and an intensity-weighted mean hydrodynamic diameter (Z-average mean) of 421 nm at pH 7. On decreasing the pH to 4.3, the zeta-potential increased to 37.6 mV, suggesting greater suspension stability, and the Z-average mean reduced to 204 nm. Although altering the pH induced a more stable dispersion, acidic and alkaline conditions can corrode Al foil commonly used as one of the current collectors, and large pH modifications were not seen as viable for direct deposition of LIB separators. Carboxymethyl cellulose (CMC) is often favored in the literature as an aqueous binder due to its relatively low environmental impact. Adding 1 wt % CMC reduced the particle Z-average mean to 220 nm. However, a zeta-potential magnitude of only −19.8 mV suggested only limited stabilization. Alternatively, poly(acrylic acid) (PAA) improved the zeta-potential magnitude to −27.0 mV and provided an acceptable Z-average mean of 225 nm after 30 min. The magnitude of polydispersity in terms of additives was in the order none > pH > CMC > PAA, i.e., a narrowing of the particle diameter distribution and the degree of agglomeration from left to right. Therefore, on the basis of the similarity of the Z-average mean and the polydispersity index (PDI), but the improved (reduced) number mean diameter and (increased magnitude) zeta-potential over CMC, PAA was selected for further experimentation.

Table 1. Zeta-Potential and Particle Diameter Analysis for the 50 nm Al_2O_3 Particles Suspended in Water Using pH Modification, PAA (1 wt %), and CMC (1 wt %)

dispersant	zeta-potential (mV)	number mean[a] (nm)	Z-average mean[b] (nm)	PDI[c]
none	15.9 ± 4.9	159	421	0.49
pH 4.3	37.6 ± 6.5	74	204	0.39
PAA	−27.0 ± 8.4	93	225	0.35
CMC	−19.8 ± 7.3	110	220	0.36

[a]Number mean diameter. [b]Intensity-weighted mean hydrodynamic diameter. [c]Polydispersity index.

Binder Optimization. Styrene−butadiene rubber (SBR) was selected as a model binder due to its known compatibility and widespread use in aqueous manufacture of LIB anodes. SBR emulsion is insoluble in water upon drying, which reduced the risk of suspension of previously deposited layers in subsequent droplets. Suspension of previously deposited material could have caused short circuits by generating pathways of conducting material (i.e., carbon black) through the separator layer during deposition. Figure 2a shows that at 2 wt % SBR the sprayed Al_2O_3 tended to flake off in small circular areas, likely caused by tensile capillary forces during drying. Figure 2b shows that when the binder was increased to 5 wt % or greater, the Al_2O_3 particles maintained adhesion to the electrode layer and substrate.

Substrate Selection. Stainless steel circular spacers from 2032 coin cells were selected as substrates to facilitate simple, punch-less assembly into standard cells. In assembling coin half-cells with an electrode and separator deposited on thin Al foil, an Li chip of diameter smaller than the separator and with exact alignment must be used to avoid short circuits. Alternatively, the use of the spacer raised the contact point of the Li foil into the middle of the cell and retained the protective conformal coating of the separator layer, removing the chance of contact between the Li foil and the cell cup or working electrode, as shown in Figure 2c. In terms of full cells, it was assumed that punching spray-deposited full cells could induce a short circuit by

https://doi.org/10.1021/acsami.2c03828
ACS Appl. Mater. Interfaces 2022, 14, 34538−34551

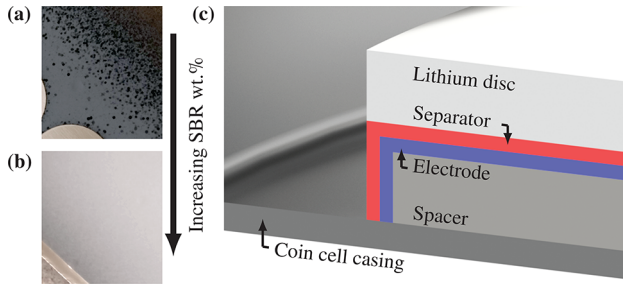

Figure 2. Optimization of binder and substrate for spray-deposited cells. Optical micrograph of Al_2O_3 nanoparticle coatings deposited onto LFP electrodes from suspensions containing (a) 2 wt % SBR and (b) 5 wt % SBR by solid mass. A spray-deposited separator half-cell with (c) the stainless steel spacer current collector creating a large separation between the lithium disc and the cell casing to avoid short circuits in test cells.

smearing material across the sides of the separator, potentially connecting the anode and cathode, and was avoided.

Solvent Optimization. A separator with a uniform structure and low roughness was desired (i.e., with no "bumps" or cracks). Separators with excessively heterogeneous structures will result in a heterogeneous current density distribution, leading to localized heating and degradation of the electrode and separator, which could lead to physical contact and short circuits between the anode and cathode.[48,49]

Figure 3a shows the surface of an Al_2O_3 separator deposited from water alone (W) onto an LFP electrode, while Figure 3b shows the surface of Al_2O_3 deposited from water with 20 vol % IPA (IPA), which had a qualitatively smoother surface. Some agglomerates persisted, most with a diameter of 1−3 μm, up to a maximum of ∼4 μm.

Surface roughness measurements of Al_2O_3 (W) and Al_2O_3 (IPA) are shown in Figures 3c and 3d, respectively, and the roughness measurements are summarized in Table 2. Table 2, consistent with the micrographs, shows that water with 20 vol % IPA gave the lowest coating roughness. The Al_2O_3 separator deposited from water alone had a lower areal density and greater thickness, which were likely due to the increased roughness. Droplets of water commonly deposit suspended particles in heterogeneous patterns due to a weak Marangoni flow during evaporation.[50] A mixture of low and high boiling point liquids can suppress the effect, which could explain the improvement gained by including 20 vol % IPA in the suspension. Overall, the physical properties of Al_2O_3 deposited from water with 20 vol % IPA were favored over that of Al_2O_3 deposited from water alone.

Three LFP half-cells with sprayed separators from each solvent mixture were assembled. The LFP half-cells with Al_2O_3 deposited from water alone could not charge due to short circuits between the anode and cathode caused by significant variations in separator thickness. In contrast, the preferred Al_2O_3 separator deposited from water with 20 vol % IPA mitigated any short circuits and was chosen for subsequent in-depth comparison with a commercial polymer separator.

3.2. Physicochemical Properties of Spray-Deposited Al_2O_3 Separators. Given their encouraging proof-of-concept demonstration when sprayed onto a cathode, spray-deposited Al_2O_3 separator physical properties, thermal stability, wettability, impedance, and electrochemical performance in LTO-based (anode) half-cells were investigated. A Celgard 2500 PP monolayer separator was used for comparative purposes.

Physical Characterization. Suspensions comprising of 50 nm Al_2O_3 particles, PAA, SBR in a 94:1:5 solid ratio, and 80:20 vol % water:IPA solvent were spray-deposited onto spacers precoated with an ∼14 μm LTO-based electrode. Figure 4 shows the resulting coated spacers, where (a) is the spacer/LTO electrode and (b−d) are spacer/LTO/Al_2O_3 electrode/separator composites, where the approximately 5, 11, and 22 μm thick Al_2O_3 separator layers are termed Al_2O_3 (5 μm), Al_2O_3 (11 μm), and Al_2O_3 (22 μm) where needed, respectively. Table 3 compares the areal density, thickness, and estimated porosity of the Al_2O_3 separators with Celgard 2500. The relatively high density of Al_2O_3 (3.95 g cm^{-3}) resulted in a higher mass per unit volume (PP density assumed at 0.9 g cm^{-3}). To obtain the same areal density, or better, than Celgard 2500, the Al_2O_3 separator should be ∼7 μm thick, i.e., approximately a third to a quarter of the Celgard thickness, assuming similar porosity. The Al_2O_3 separator porosity was estimated as 58 ± 3, 59 ± 5, and 60 ± 10% for 22, 11, and 5 μm thickness, respectively, slightly higher than that of Celgard 2500.[51,52]

Figures 5a and 5b show SEM cross-sectional images of ∼14 μm LTO electrodes coated with 5 and 22 μm thick Al_2O_3 separators. The Al_2O_3 separator coated conformally onto the

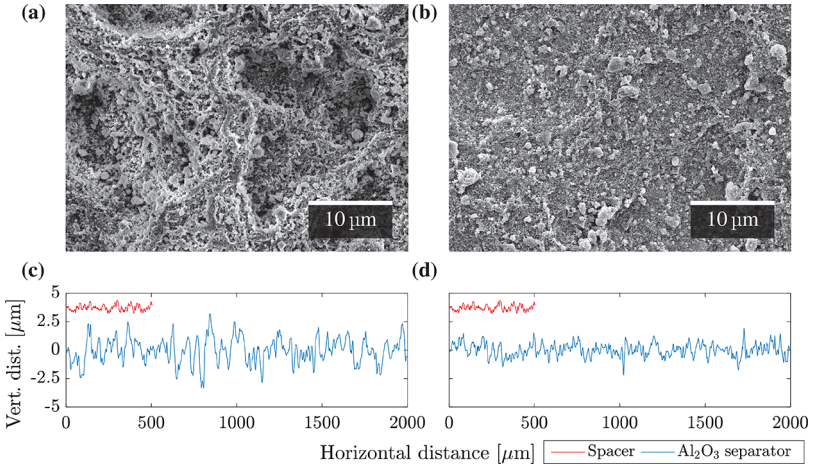

Figure 3. Plan-view SEM micrographs of Al_2O_3 layers deposited on top of sprayed LFP-based electrodes and corresponding surface profiles. Al_2O_3 was deposited from (a) water and (b) water:IPA 80:20 vol % suspensions containing 1 wt % PAA and 5 wt % SBR of the total solid mass. Surface profiles of (a) and (b) are displayed in (c) and (d), respectively.

https://doi.org/10.1021/acsami.2c03828
ACS Appl. Mater. Interfaces 2022, 14, 34538−34551

Table 2. Physical Properties of Oxide Separators, Al_2O_3 Deposited from Water Alone (W), and Al_2O_3 Deposited from Water with 20 vol % Isopropyl Alcohol (IPA)[a]

separator	R_a (μm)	W_a (μm)	max(P2V) (μm)	areal density (mg cm^{-2})	thickness (μm)	FC
Al_2O_3 (W)	0.5	1.0 ± 0.3	5.3 ± 0.8	1.59 ± 0.05	12 ± 1	0/3
Al_2O_3 (IPA)	0.3	0.7 ± 0.2	3.7 ± 0.7	1.70 ± 0.05	11 ± 1	3/3

[a]R_a is the arithmetic average deviation from the mean line, W_a is the arithmetic average deviation of waviness from the mean line, and max(P2V) is the largest height difference between a neighboring peak and valley. The functional cells (FC) column lists how many of three assembled cells were able to charge and discharge on the first cycle.

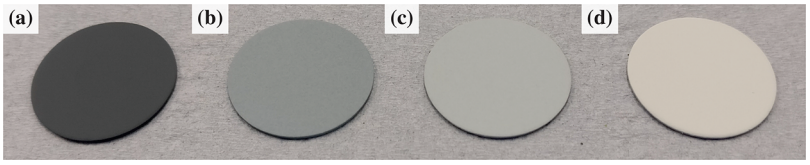

Figure 4. Stainless steel spacers coated with (a) an LTO electrode layer and (b–d) an LTO electrode layer coated with a 5, 11, and 22 μm thick Al_2O_3 separator layer, respectively.

Table 3. Comparison of the Thickness, Mass, Estimated Porosity, and Pore Size of a Celgard 2500 Separator and Three Spray-Deposited Al_2O_3-Based Separators of Varying Thickness[51,52]

separator	AD[a] (mg cm^{-2})	d^b (μm)	porosity (%)	pore size (μm)
Celgard	1.13 ± 0.04	25 ± 1	55	0.21 × 0.06
Al_2O_3 (5 μm)	0.74 ± 0.05	5 ± 1	60 ± 10	
Al_2O_3 (11 μm)	1.70 ± 0.05	11 ± 1	59 ± 5	
Al_2O_3 (22 μm)	3.44 ± 0.05	22 ± 1	58 ± 3	

[a]Areal density. [b]Thickness.

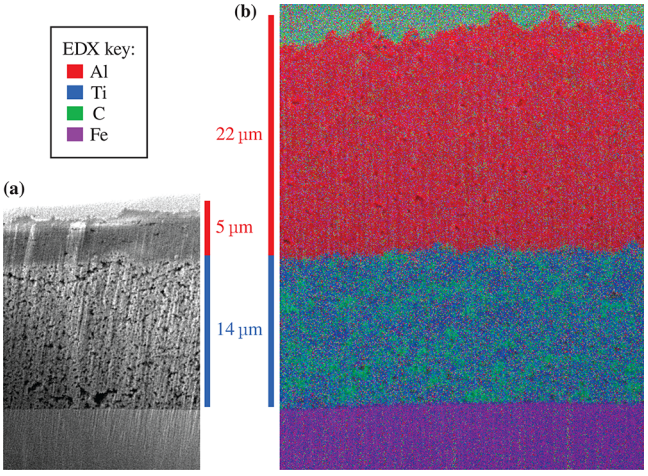

Figure 5. Cross-sectional SEM images of LTO-based electrodes coated with (a) Al_2O_3 (5 μm) and (b) Al_2O_3 (22 μm) with an overlaid EDX map. From bottom to top, the layers are the stainless steel spacer (purple), the LTO (blue) and carbon black (green) electrode, the Al_2O_3 separator (red), and the Pt/C coating layer.

underlying sprayed LTO-based layer. From Figure 5a,b, Al_2O_3 (5 μm) had an estimated deviation from the mean line of ±1 μm, while Al_2O_3 (22 μm) was slightly rougher at ∼±2 μm. Al_2O_3 (5 μm) had a few large pores of diameters of 200–300 nm, while Al_2O_3 (22 μm) had pores with diameters up to ∼400 nm.

Nitrogen gas surface adsorption (BET) was used to investigate the specific surface area and mesoporosity of Al_2O_3 separator layers on Al foil. A separator layer fabricated from 300 nm Al_2O_3 particles was manufactured to provide additional comparison. A separator consisting of 300 nm Al_2O_3 was unable to hold charge when tested in LFP half-cells, suggesting that particle size (or pore diameter) was likely a critical factor when successfully fabricating spray-deposited separators.

The BET isotherms of the Celgard and separators fabricated by using 50 nm Al_2O_3 and 300 nm Al_2O_3 are shown in Figure 6a. Celgard and the separator using 50 nm Al_2O_3 displayed a hybrid shape between a classical type II and type IVa behavior,[53] comprising adsorption–desorption hysteresis.

According to IUPAC, type II behavior is typical of nonporous or macroporous solids, as multilayer formation of adsorbed nitrogen appears to increase without limit as p/p° tends to 1. A type IVa isotherm is typical of mesoporous solids and is generated due to pore condensation, where the adsorbing gas condenses to a liquidlike state at a pressure below p°. However, a final saturation plateau, typical of a type IVa, was not observed, indicating a structure with both mesoporosity and macroporosity.[53]

H1 hysteresis is usually associated with a narrow range of uniform pores. However, it has also been attributed to spherical/cylindrical pore structures with wide openings through which there is immediate access to the vapor phase.[53,54] The distinctive isotherm of the separator using 50 nm Al_2O_3 likely represents a porous powder bed with little or no pore blocking, similar to isotherms of nonporous nanoparticles.[55–57]

The specific surface area (SSA) was calculated from the BET isotherms and is shown in Table 4. For the separator using 300 nm Al_2O_3 SSA = 9.4 m^2 g^{-1} with no distinctive hysteresis loop, indicating little or no mesoporosity. For the separator using 50 nm Al_2O_3 SSA = 44.4 m^2 g^{-1}, while for Celgard SSA = 41.3 m^2 g^{-1}. The separator using 50 nm Al_2O_3 had an estimated density of 3.77 g cm^{-3}, ∼4 times greater than that of Celgard at 0.9 g cm^{-3}, so the difference in the surface area per unit volume was much higher than Table 4 suggested. A high surface area could increase electrolyte uptake but may also increase chemical side reactions.

Figure 6c shows that the separator using 300 nm Al_2O_3 had little mesoporosity, represented by a low cumulative mesopore volume of 0.01 cm^3 g^{-1}. The cumulative mesopore volume of the Celgard and the separator using 50 nm Al_2O_3 were 0.28 and 0.20 cm^3 g^{-1}, respectively. The Celgard separator showed a narrower pore width distribution (PWD) with an average pore width of 22 nm. The separator using 50 nm Al_2O_3 had an average pore width

https://doi.org/10.1021/acsami.2c03828
ACS Appl. Mater. Interfaces 2022, 14, 34538–34551

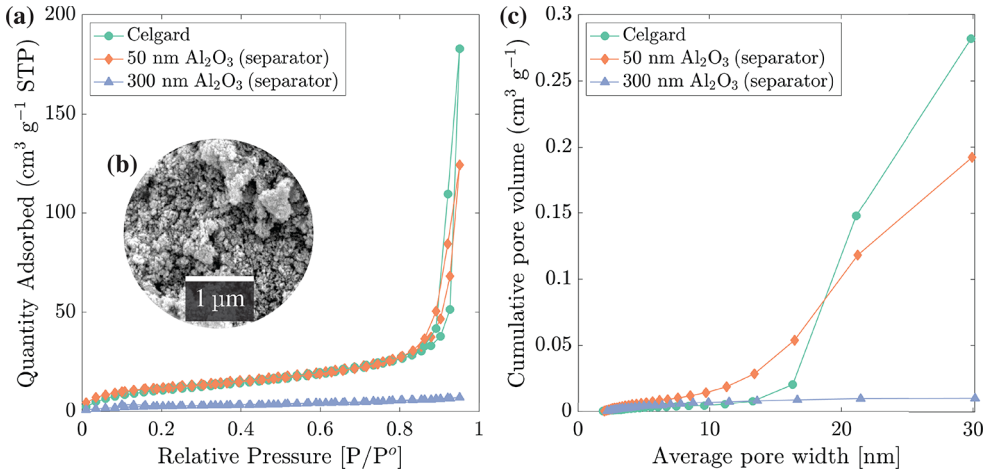

Figure 6. Nitrogen gas adsorption measurements and calculations for Celgard 2500 and separators fabricated by using 50 nm Al_2O_3 and 300 nm Al_2O_3. (a) BET isotherms, (b) micrograph of the separator using 50 nm Al_2O_3, and (c) BJH desorption cumulative average pore width distributions.

Table 4. Comparison of the Specific Surface Area of the Celgard Separator and the Separators Using 50 and 300 nm Al_2O_3 and the Calculated Proportion of Pore Widths in the Celgard and Separator Using 50 nm Al_2O_3[a]

separator	SSA (m^2 g^{-1})	V_{sep}	V_{solid}	V_{pore}	V_{meso}	V_{macro}	$V_{meso,\%}$	$V_{macro,\%}$
300 nm Al_2O_3	9.4							
Celgard	41.3	2.47	1.11	1.36	0.28	1.08	21	79
50 nm Al_2O_3	44.4	0.60	0.27	0.34	0.20	0.14	59	41

[a]On a per gram basis, V_{sep} is the volume of the separator, and V_{solid}, V_{pore}, V_{meso}, and V_{macro} are the volumes occupied by the solid, total porosity, mesopore, and macropore components of the separator, respectively, with units of cm^3 g^{-1}. $V_{meso,\%}$ and $V_{macro,\%}$ are the percentage of total porosity credited to meso and macropores, respectively.

of 17 nm and a broader PWD in the mesopore range, with minimum pore widths of <10 nm.

To estimate the volume of each component in the separators, a simple relation was used:

$$V_{sep} = V_{solid} + V_{meso} + V_{macro} \quad (2)$$

where, on a per gram basis, V_{sep} is the volume of the separator, and V_{solid}, V_{meso}, and V_{macro} are the volumes occupied by the solid, mesopore, and macropore components of the separator, respectively, as shown for the Celgard and Al_2O_3 separators in Table 4. Table 4 reinforces some important comparisons between the separator using 50 nm Al_2O_3 and Celgard. Celgard had a significantly larger pore volume per gram of material (V_{pore}) of 1.36 cm^3 g^{-1} compared with that of Al_2O_3 at 0.34 cm^3 g^{-1}, displaying an advantage of polymer-based separators. The ratio of mesopores to macropores was 0.59:0.41 for the separator using 50 nm Al_2O_3, compared with 0.21:0.79 for the Celgard separator. The proportion of mesopores in the separator using 50 nm Al_2O_3, assuming a monomodal pore distribution, suggested a fine-scale average pore width near that of the average particle diameter of ~50 nm.

Temperature Stability. Figure 7 shows TGA plots for the Celgard 2500 separator (Celgard), poly(acrylic acid) (PAA), styrene−butadiene rubber (SBR), 300 nm Al_2O_3 and 50 nm Al_2O_3 powders, and the spray-deposited separator using 50 nm Al_2O_3 between 25 and 900 °C. Figure 7a,b shows that PP decomposed in a single step at 252 °C, with a maximum rate of degradation (DTG peak) at 387 °C, and was fully degraded at 482 °C. Poly(acrylic acid) displayed four distinct DTG peaks, with three well-documented high-temperature peaks.[58−60] The first peak (2% mass loss at 50−130 °C) was simply evaporation of absorbed water. Stage 1 of polymer decomposition (mass loss of 11% at 160−280 °C with a peak at 240 °C) was attributed to reversible anhydride formation.[61] Stage 2 (mass loss of 22% with a peak at 330 °C) was due to decarboxylation of the anhydride and release of CO_2. Finally, a broad peak, related to chain scission of the polymer, occurred above 350 °C, and led to a further mass loss of 55%. A mass of 10% carbonaceous residue remained above 530 °C. Styrene−butadiene rubber decomposed in a single step between 320 and 520 °C with a DTG peak at 460 °C and left a residual mass of 4.5%. The small peak at 150 °C was most likely due to volatilization of processing additives.[62]

The 300 nm Al_2O_3 powder in Figure 7c maintained 99.6% mass up to 900 °C. The 50 nm Al_2O_3 powder reduced in mass gradually to 95.3% at 900 °C. Figure 7d shows the normalized mass loss against temperature (upper traces, left axis) and the DTG (lower traces, right axis). Both 50 and 300 nm Al_2O_3 powders lost mass below 100 °C, which was attributed to evaporation of physically adsorbed water. In terms of normalized mass loss, both powders lost 35% of their total mass loss below 100 °C and followed similar trends up to 900 °C. An equilibrium between aluminum oxide−hydroxides and Al_2O_3 occurs at ~370 °C (below 200 bar), and this may be evident in the DTG of 50 nm Al_2O_3 and the normalized mass loss of 300 nm Al_2O_3.[63] Therefore, the slight differences between the Al_2O_3 powders above 150 °C were most likely due to slightly different hydroxide surface species, and overall the mass loss of 50 nm Al_2O_3 powder was as expected.

The optimized Al_2O_3 separator comprised a 94:1:5 composite of 50 nm Al_2O_3 particles, PAA and SBR, and displayed similar mass loss behavior to 50 nm Al_2O_3 powder until 300 °C, along with some underlying degradation of the small quantity of the PAA consistent with Figure 7a,b. There were two large decomposition peaks in Figure 7d, at 420 and 600 °C, the last

https://doi.org/10.1021/acsami.2c03828
ACS Appl. Mater. Interfaces 2022, 14, 34538−34551

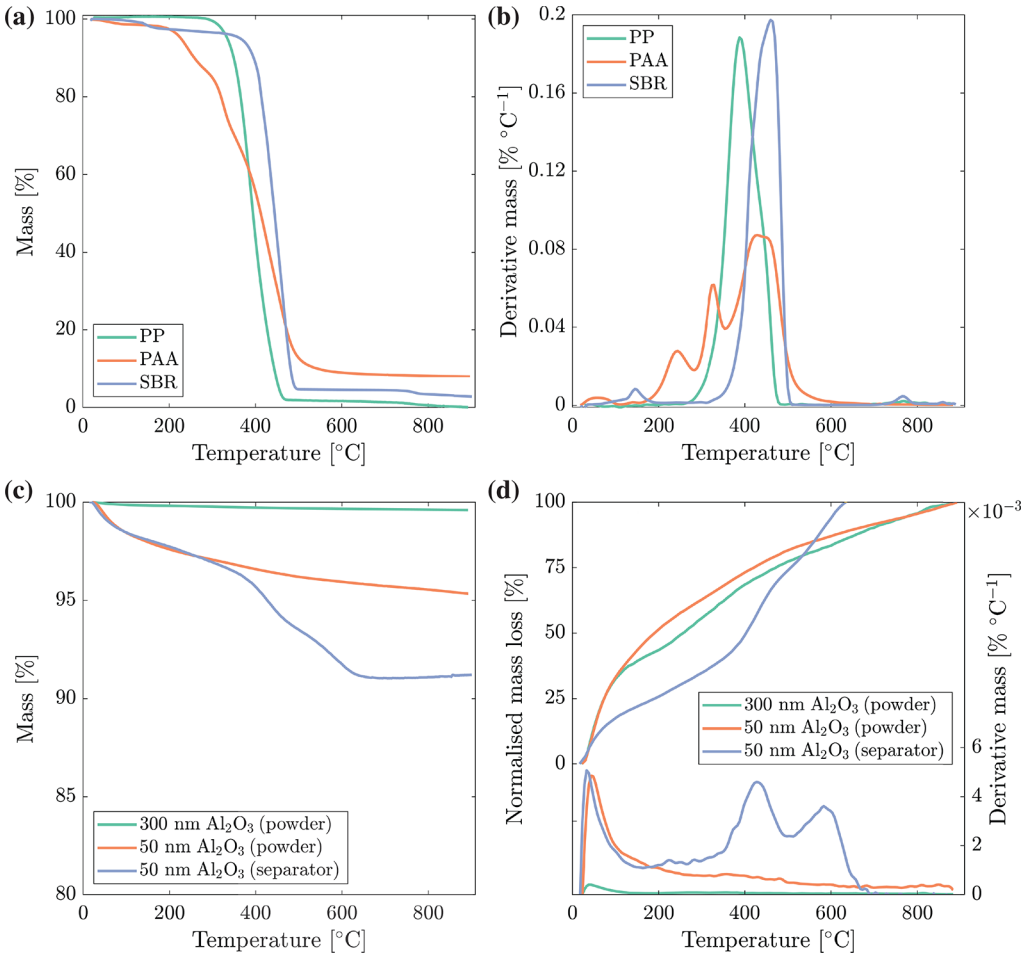

Figure 7. Thermogravimetric analysis of a Celgard 2500 separator and a spray-deposited Al_2O_3 separator and requisite materials between 25 and 900 °C. (a) TGA and (b) DTG of Celgard 2500 (PP), poly(acrylic acid) (PAA), and styrene−butadiene rubber (SBR). (c) TGA, (d, upper) normalized mass loss, and (d, lower) DTG of 300 nm Al_2O_3 powder, 50 nm Al_2O_3 powder, and spray-deposited Al_2O_3 separator using 50 nm Al_2O_3 particles.

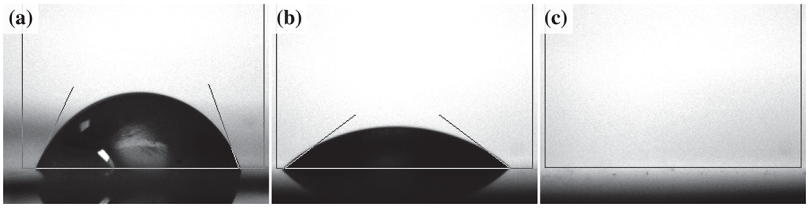

Figure 8. Contact angle measurements of ethylene carbonate (EC) and dimethyl carbonate (DMC) in a 50/50 v/v mixture dropped onto (a) Celgard 2500, (b) a stainless steel spacer, and (c) a stainless steel spacer coated with the spray-deposited Al_2O_3 separator.

of which in particular was not previously resolved in the individual constituent materials. Decomposition continued until a temperature (~720 °C) higher than the polymers by themselves (620 °C), potentially due to the reduced thermal conductivity of the composite separator or the degradation of some new species formed between the Al_2O_3, the Al_2O_3 surface species, and/or one or more of the polymer components at lower temperature. At 900 °C, the 50 nm Al_2O_3 powder had 95.3% of original mass remaining, while the separator using 50 nm Al_2O_3 retained 91.2%. This difference was slightly less than expected from the 6 wt % of PAA and SBR combined in the oxide separator but lies within the likely error of the technique.

Electrolyte Wetting. The performance of separators relies significantly on their wettability with the electrolyte.[10,64,65] A high contact angle (poor wetting) is usually expressed as a relatively high electrolyte resistance across the separator and unfilled pores may result. Figure 8 shows contact angle measurements of a 50/50 v/v mixture of ethylene (EC) and dimethyl carbonates (DMC) on the Celgard 2500 separator, a stainless steel spacer, and a stainless steel spacer coated with a separator using 50 nm Al_2O_3, with contact angles of 64.9 ± 5.5°, 35.8 ± 1.2°, and ~0°, respectively. A coating of 50 nm Al_2O_3 only 5 μm thick reduced the contact angle of the spacer from 36° to ~0°.

3.3. Electrochemical Properties of Spray-Deposited Al_2O_3-Based Separators.

Separator Impedance. Figure 9a shows Nyquist plots from electrochemical impedance spectroscopy (EIS) to estimate the effective ionic conductivities of

https://doi.org/10.1021/acsami.2c03828
ACS Appl. Mater. Interfaces 2022, 14, 34538−34551

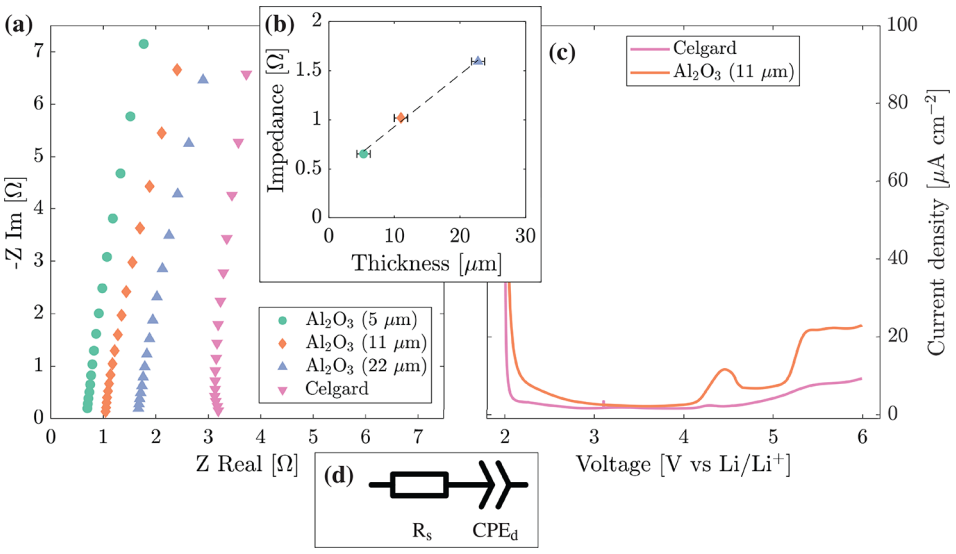

Figure 9. Impedance spectroscopy and linear voltage sweep response of separators soaked in a 1.0 M $LiPF_6$ EC/DMC 50/50 v/v electrolyte. (a) Impedance spectroscopy between 10 and 200 kHz for Celgard and 5, 11, and 22 μm thick Al_2O_3 separators, (b) the relationship between equivalent series resistance and Al_2O_3 separator thickness, (c) linear voltage sweeps for Celgard and the 11 μm thick Al_2O_3 separator, and (d) the equivalent circuit used to estimate the equivalent series resistance from (a).

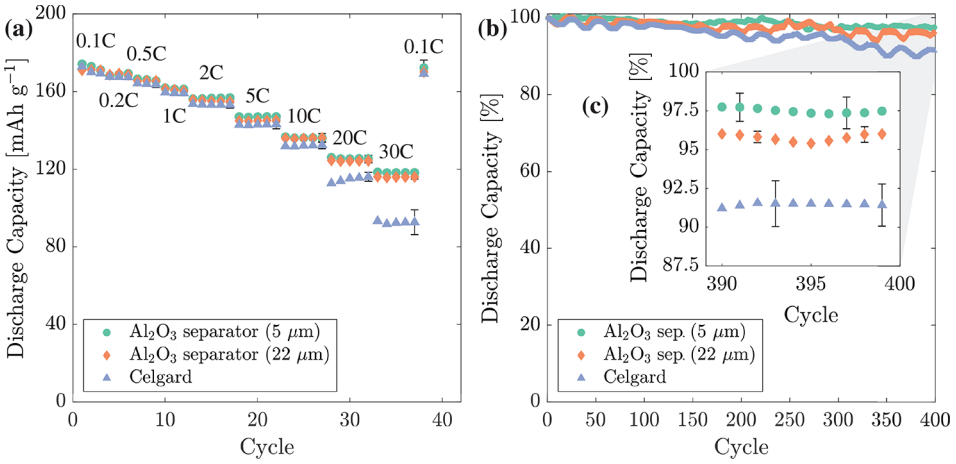

Figure 10. Comparison of LTO half-cell performance using Celgard or Al_2O_3 separators: (a) cycling performance between 0.1 and 30 C, (b) long-term cycling at 2 C for 400 cycles, and (c) a magnified inset of the last 10 cycles in (b).

electrolyte soaked separators in spacer/separator/spacer coin cells. From this point, all Al_2O_3 separators were fabricated with 50 nm Al_2O_3. The equivalent series resistance, determined by modeling the impedance response by using Figure 9d, was 0.35, 0.54, 0.84 and 1.62 Ω cm^{-2} for 5, 11, and 22 μm thick Al_2O_3 separators and a Celgard separator. Figure 9b plots the equivalent series resistance against the separator thickness and shows an approximately linear relationship for the Al_2O_3 separators. The effective ionic conductivity of the Al_2O_3 separators was estimated as 0.98 $\pm$ 0.05 mS cm^{-1}, roughly double that of Celgard 2500 of 0.50 mS cm^{-1}. The higher ionic conductivity and lower equivalent series resistance were attributed to the superior wettability of the Al_2O_3 separator.

Electrochemical Stability. The stability of the separators under electrochemical conditions was studied by using linear sweep voltammetry on spacer/separator/spacer coin cells in 1 M $LiPF_6$ EC/DMC 50/50 v/v electrolyte, as shown in Figure 9c. The Celgard separator showed a current density of ~1.7 μA cm^{-2} up to 4 V and then a continual rise in current density after ~4.5 V. The small peak in current density at 4.2−4.3 V was due to the oxidation of water (based on the standard hydrogen potential).[66,67] The current density of the Al_2O_3 separator cell up to 4 V was ~2.4 μA cm^{-2}, slightly higher than that of the Celgard separator cell.

The water oxidation peak for the Al_2O_3 separator cell was relatively large at 11.6 μA cm^{-2} over 4.2−4.6 V and was likely due to the difficulty in removing excess water from the hydrophilic PAA dispersant and high surface area Al_2O_3 particles. The current density of the Al_2O_3 separator cells reduced to 7.5 μA cm^{-2} at ~5 V, close to 4.5 μA cm^{-2} of the Celgard separator cells. Above 5.1 V, the current density for the Al_2O_3 separator was ~2 times that of Celgard. Overall, the Al_2O_3 separator displayed adequate voltage stability up to 5 V, but there may be room for further improvement with the use of more stable polymer binders and improved drying procedures.

Galvanostatic Cycling. The performance of LTO/separator/Li half-cells containing Al_2O_3 (5 μm), Al_2O_3 (22 μm), and Celgard were investigated between 0.1 and 30 C, as shown in Figure 10a. The 5 and 22 μm thick Al_2O_3 separators produced consistent capacities with a maximum difference in capacity of

https://doi.org/10.1021/acsami.2c03828
ACS Appl. Mater. Interfaces 2022, 14, 34538−34551

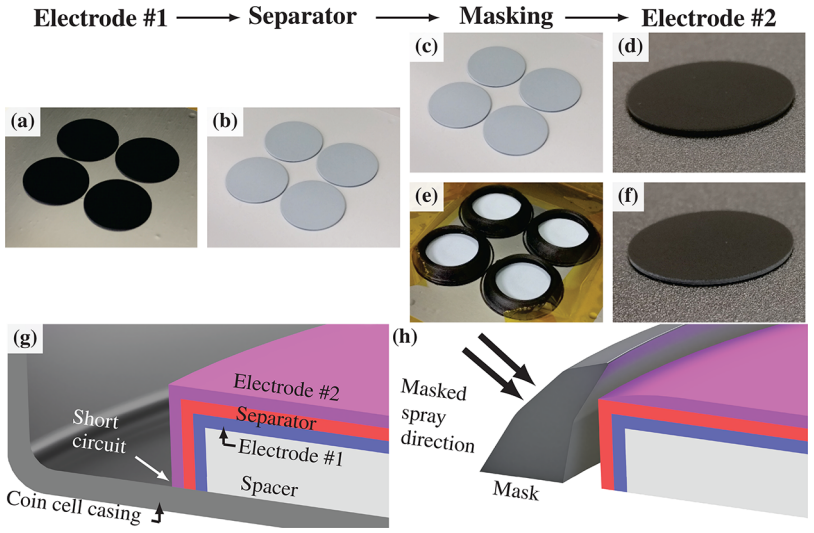

Figure 11. Process of manufacturing sequentially spray-deposited full cells: (a) initial electrode layer deposition onto spacers, (b) Al_2O_3 separator layer deposition, (c) second electrode deposition without mask, (d) final full cell with a conformal second electrode, (e) second electrode deposition with 3D printed masks, and (f) final full cell with second electrode restricted from conformal coating. Schematic cross sections of (g) the full cell without second electrode layer masking and (h) the full cell with second electrode layer masking and the masking process.

2% at 30 C. Between 0.1 and 10 C, all types of separators facilitated an initial discharge capacity of 170 ± 2 mAh g^{-1}, with the largest difference in capacity of only 2.8% between the Al_2O_3 separators (136.2 ± 1.0 mAh g^{-1}) and the Celgard separator (132.5 ± 1.9 mAh g^{-1}) at 10 C. However, at higher rates, Al_2O_3 (5 μm) outperformed Celgard by 8.1% with a capacity of 125.5 ± 1.0 mAh g^{-1} compared with 116.1 ± 2.3 mAh g^{-1} at 20 C and by 27.8% with a capacity of 118.3 ± 1.2 mAh g^{-1} compared with 92.5 ± 6.4 mAh g^{-1} at 30 C. Similarly, Al_2O_3 (22 μm) was within ±2 mAh g^{-1} of Al_2O_3 (5 μm) at all tested C rates. The Al_2O_3 separators evidenced a relatively low standard deviation between cells, which arose due to their excellent wetting and fine-scale microstructural uniformity.

Cycle stability was assessed at 2 C over 400 cycles, as shown in Figure 10b. All cells had an initial capacity of ~155 mAh g^{-1} at 2 C on the first cycle (assumed as 100% capacity). After 400 cycles, Al_2O_3 (5 μm), Al_2O_3 (22 μm), and Celgard retained capacities of 97.5 ± 0.9, 96.0 ± 0.4, and 91.5 ± 1.4%, with a capacity loss per cycle of 0.0068, 0.0093, and 0.0210%, respectively. The 2−3 times greater capacity retention for cells using Al_2O_3 separators was again ascribed to their significantly lower impedance and improved wetting.

It is worth recalling that the sprayed electrodes in the half-cells tested here were not calendared. Nonetheless, even the 5 μm thick Al_2O_3 separator provided consistent, high performance enabled by the excellent conformal coating and even coverage.

3.4. Physical and Electrochemical Properties of Full Cells. Previous work has shown two advantageous properties of spray deposition: (1) the ability to process multiple layers in a continuous operation, due to "on-the-fly" changing of deposition conditions and incremental drying of layers,[42,43,68,45] and (2) conformal coating of presprayed substrates. Combining these attributes could enable coating of LIBs onto a variety of substrates, including nonflat geometries.

Figure 11 shows the processing steps for manufacturing Li-ion full cells by spray deposition: (a) electrode #1 (LTO-based) was deposited onto spacers, (b) an Al_2O_3 separator was deposited onto electrode #1, (e) 3D printed masks were positioned over the LTO/Al_2O_3-coated spacers, and (f) electrode #2 was deposited onto masked LTO/Al_2O_3. Figure 11c,d shows how deposition without masks resulted in conformal coating of electrode #2 onto the side of the LTO/Al_2O_3-coated spacers, leading to short circuits on cell assembly, as shown in the schematic diagram in Figure 11g. Figure 11f shows the separator layer on the side of the spacer visible even after deposition of electrode #2, which prevented shorting because of the masking arrangement shown schematically in Figure 11h.

Cross sections of an Al_2O_3 separator full cell were examined by SEM imaging and EDX analysis, as shown in Figure 12. Ti (blue) differentiated the LTO, Al (red) the Al_2O_3 separator, Fe (purple) the LFP and stainless steel spacer, and C (green) in both the LTO (anode) and LFP (cathode). In this case the LTO-based layer had slightly larger variations in thickness of up to 4 μm. Nonetheless, the 10 μm Al_2O_3 separator layer conformally adopted the surface topography. The LTO/separator interface had excellent contact while the separator/LFP interface had some pores of 2−3 μm diameter.

Figure 12b,c displays magnified cross sections of (b) the LTO/separator interface and (c) the separator/LFP interface. Overall, all the layers showed remarkably good particle packing and consistency of microstructure given the absence of calendering.

Figure 13a shows full cell rate testing performed between 0.1 and 30 C, with discharge capacity determined in terms of the LFP cathode for both the Al_2O_3 separator full cells and conventional full cells using a polypropylene Celgard 2500 separator. The cells were fabricated with an LFP:LTO capacity ratio of 1:1 according to 0.1 C capacities measured previously, and all electrodes were manufactured by using spray deposition. The Celgard full cells had a capacity of 137.2 ± 0.4 mAh g^{-1} at 0.1 C, while those with a Al_2O_3 separator had a similar capacity of 136.3 ± 0.8 mAh g^{-1}. Between 5 and 30 C, the Celgard 2500 separator enabled a greater capacity at the start of each set of five cycles, but capacity reduced each cycle. On the other hand, the cells using a Al_2O_3 separator increased in capacity during each set of cycles until capacities were almost equal. After 30 C, Celgard and Al_2O_3 separator full cells recovered to capacities of 134.8 ± 0.5 and 136.2 ± 0.8 mAh g^{-1} at 0.1 C, respectively.

https://doi.org/10.1021/acsami.2c03828
ACS Appl. Mater. Interfaces 2022, 14, 34538−34551

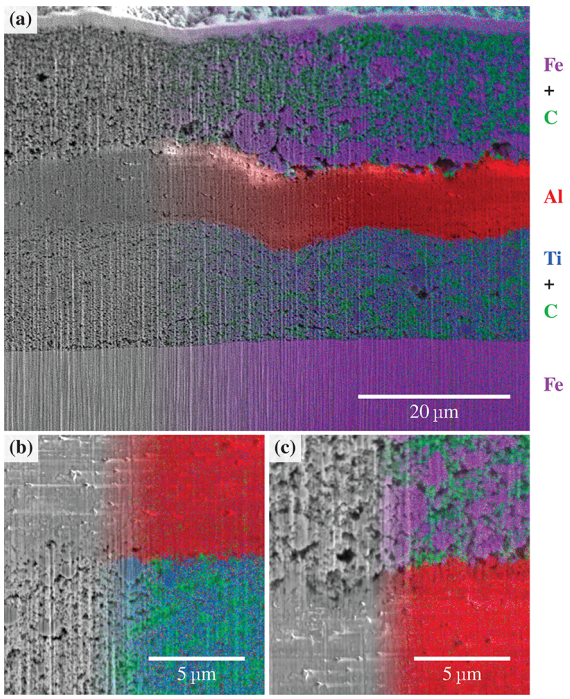

Figure 12. Cross-sectional SEM image of a spacer/LTO/Al_2O_3 separator/LFP cell assembly with an overlaid EDX map on the right-hand side of each image. The layers measure approximately 14.8 ± 2, 9.7 ± 0.7, and 17.7 ± 1.7 μm in thickness for LTO, Al_2O_3 separator, and LFP, respectively. The EDX element color key is displayed on the right of the image.

Cycle stability was examined over 400 cycles at 2 C directly after the rate testing. Celgard and Al_2O_3 separator full cells had initial capacities of 108.6 ± 1.5 and 109.0 ± 1.3 mAh g^{-1}, reducing to 86.0 ± 1.4 and 104.9 ± 1.9 mAh g^{-1} after 400 cycles. The average Coulombic efficiency of each cell was 99.8%. After 400 cycles, Celgard and Al_2O_3 separator full cells had final capacities of 79.2 ± 1.3 and 96.3 ± 1.8% and a capacity loss per cycle of 0.0354 and 0.0106%, respectively.

Relating the degradation of Celgard full cell capacity to that of LTO/Celgard half-cells (Figure 10), the capacity loss per cycle calculated by linear regression for Celgard full cells was almost 1.7× greater over 400 cycles. The capacity loss per cycle of full cells with a 10 μm thick Al_2O_3 separator after 400 cycles, 0.0106%, was slightly larger than 5 and 22 μm thick Al_2O_3 separator half-cells with 0.0068 and 0.0093%, respectively. However, the capacity of the LFP was intrinsically less stable than the LTO under long-term cycling, so a poorer capacity retention in the LFP/LTO full cells was expected.

Overall, the best sprayed Al_2O_3-based separators performed at least as well as the commercial Celgard polymer separator, but with notable improvements in cell capacity retention in integrated full cells and high C-rate response in LTO half-cells. A significant reduction in separator thickness was evidenced for the integrated full cell compared to previous literature (from 200 to 5−10 μm).[41] Several optimizations have been suggested to contribute to the effectiveness of the sprayed Al_2O_3 separators. The mixed carrier liquid improved uniformity of deposited particles by influencing droplet evaporation, the small average separator pore size (50 nm) blocked penetration of conducting material from the second electrode layer or Li metal, and the combination of high substrate temperature and the addition of SBR emulsion stabilized layers of separator material upon deposition. The Al_2O_3 separator in the full cell assembly was thinner than the Celgard separator, which contributed to the difference in capacity retention partly. However, as shown in Figure 10b, the Al_2O_3 separator with similar thickness to the Celgard separator displayed significantly better capacity retention in a half-cell configuration. Therefore, it is suggested that the principal reason for the slower degradation of the Al_2O_3 separator containing cells is their intrinsic improved wetting of the electrolyte (Figure 8) and lower impedance (Figure 9). The lower impedance reduces the required overpotentials to drive electrochemical energy storage reactions, and so degradation by unwanted side-reactions that may occur at elevated potentials and temperatures is somewhat reduced.

The spray deposition route can also be used to fabricate successfully LIB anodes and cathodes from a variety of different active materials, including those with particles diameters of up to 20 μm. When using larger diameter particles for spray-deposited three-layer full cells in a single operation, i.e., similar to the LFP/Al_2O_3/LTO cells fabricated here, the unavoidable increase in surface roughness associated with larger diameters can cause

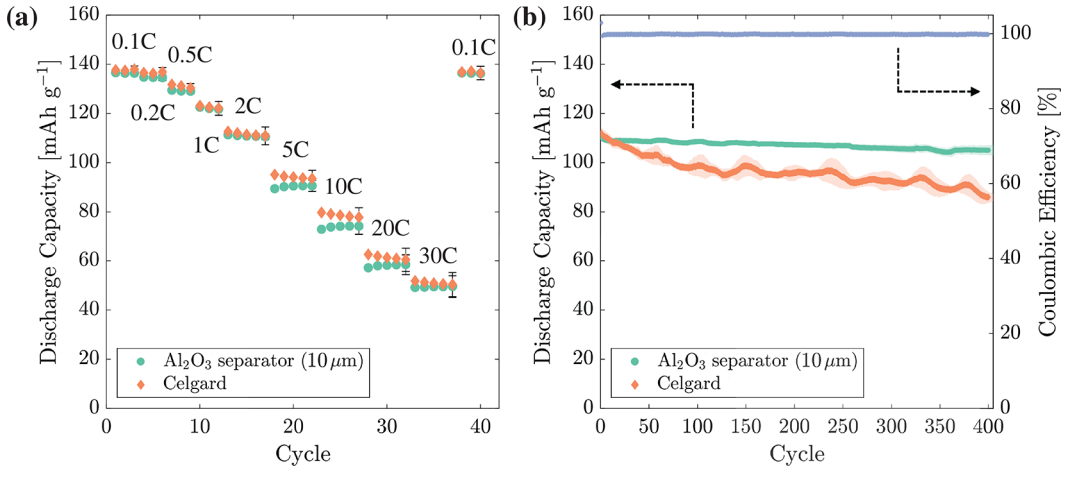

Figure 13. Electrochemical rate and cycling testing of spacer/LTO/separator/LFP full cells displaying discharge capacity of the LFP electrode. (a) Rate testing of full cells manufactured by using continuous spray deposition with an Al_2O_3 separator or conventional assembly using a polypropylene Celgard 2500 separator between 0.1 and 30 C. (b) Cycle stability of cells over 400 cycles at 2 C.

https://doi.org/10.1021/acsami.2c03828
ACS Appl. Mater. Interfaces 2022, 14, 34538−34551

difficulties in ensuring the subsequent sprayed separator layer provides an unbroken electron barrier of approximately constant thickness over the entire electrode area. The most effective approach to this challenge is to introduce an intermediate calendaring step that effectively smooths the sprayed surface (as well as providing some electrode densification). Although this undermines some of the single operation benefits of the current arrangements, it is relatively simple and effective to implement. For convenience, the spray deposition process is normally operated with aqueous based suspensions/solvents, although it can also be successfully implemented in an inert, dry atmosphere by using organic solvents for more air/water sensitive active materials. Solid electrolytes have also been successfully codeposited for hybrid solid state cathodes and separators based on ion-conducting polymers and inorganic electrolytes.[44,69] The ability to control surface topography to mitigate separator defects is also useful as larger area electrodes and one-step cells are fabricated in scale-up investigations. In this ongoing work, calendering is also used to add the top-layer or "upper" current collector with sufficient cycle life stability and low impedance, for example, by warm rolling of an Al foil precoated with a thin layer of thermopolymer onto the three-layer assembly.[70] However, it should be noted that calendering of multilayers (as opposed to calendering layer by layer) may develop a tendency for short circuits to form across the separator should there be regions of unusually high surface roughness.

4. CONCLUSIONS

Spray-deposited Al_2O_3-based separators enabled stable, high rate, and long-term cycling of LTO/Li and LFP/LTO cells. Initial optimization of dispersant, binder, and solvent for spray-deposited separators assessed suspension stability and deposition properties. An optimized Al_2O_3-based separator contained 1 wt % PAA and 5 wt % SBR and was deposited from an aqueous suspension containing 20 vol % IPA. Al_2O_3 separator surface morphology was more uniform with a 20 vol % IPA solvent than with water alone, attributed to a greater Marangoni flow during droplet drying that more efficiently distributed the 50 nm particles into a relatively uniform layer.

Al_2O_3 separators between 5 and 22 μm thick had consistent and similar porosity of ∼58%, excellent wettability (contact angle ∼0°), thermal stability to at least 180 °C, adequate electrochemical stability, and high ionic conductivity of 0.98 mS cm^{-1}, double that of a commercial PP separator. Furthermore, LTO half-cells with 5 and 22 μm Al_2O_3 separators showed improved rate performance and excellent cycle stability (0.007−0.009% capacity fade per cycle) compared with Celgard 2500 (0.021% capacity fade per cycle) due to the improved compatibility of the electrolyte and separator.

A full cell manufactured in a sequential spray process with a 10 μm Al_2O_3 separator, the first of its kind, showed similar rate performance to a conventional Celgard 2500 full cell with a capacity of ∼50 mAh g^{-1} at 30 C. Upon long-term cycling at 2 C, the Al_2O_3 separator full cells displayed excellent capacity retention per cycle of 0.0106% over 400 cycles compared with 0.0354% for the full cells with a Celgard separator. After 400 cycles, Al_2O_3 and Celgard separator full cells retained ∼96 and ∼79% of their initial 2 C capacity due to the lower impedance of the Al_2O_3 separator in the full cell assembly.

Further avenues to improve the oxide separator performance include selecting particles with lower density, improving the separator drying step, and using a dispersant with better dispersive and thermal properties than PAA. Nonetheless, this work showed that a single deposition technique can be used to process both electrodes and separators for Li-ion batteries and that cells manufactured by using this assembly technique can have similar or greater performance than those assembled with a conventional PP separator.

AUTHOR INFORMATION

Corresponding Authors

Jack D. Evans − *Department of Materials, University of Oxford, Oxford OX1 3PU, U.K.; The Faraday Institution, Didcot OX11 0RA, U.K.;* orcid.org/0000-0001-5363-4857; Email: jackevans92@gmail.com

Yige Sun − *Department of Materials, University of Oxford, Oxford OX1 3PU, U.K.; The Faraday Institution, Didcot OX11 0RA, U.K.;* orcid.org/0000-0001-8661-8642; Email: yige.sun@materials.ox.ac.uk

Patrick S. Grant − *Department of Materials, University of Oxford, Oxford OX1 3PU, U.K.; The Faraday Institution, Didcot OX11 0RA, U.K.*; Email: patrick.grant@materials.ox.ac.uk

Complete contact information is available at: https://pubs.acs.org/10.1021/acsami.2c03828

Notes

The authors declare no competing financial interest.

ACKNOWLEDGMENTS

J.D.E. received funding from the UK Engineering and Physical Sciences Research Council (Award reference 1653563) and Faraday Institution (Grant number FIR015). Y.S. received funding from UK Engineering and Physical Sciences Research Council (Grant EP/M009521). The authors thank Dr. Colin Johnston and Nicola Flanagan from the Oxford Materials Characterisation Service for help with TGA and BET data collection.

REFERENCES

(1) Lee, H.; Yanilmaz, M.; Toprakci, O.; Fu, K.; Zhang, X. A Review of Recent Developments in Membrane Separators for Rechargeable Lithium-Ion Batteries. *Energy Environ. Sci.* **2014**, *7* (12), 3857−3886.

(2) Kang, G.-d.; Cao, Y.-m. Application and Modification of Poly(Vinylidene Fluoride) (PVDF) Membranes − A Review. *J. Membr. Sci.* **2014**, *463*, 145−165.

(3) Wei, X.; Haire, C. Biaxially Oriented Microporous Membrane. Celgard LLC; US Patent US8795565B2, August 2007.

(4) Lu, W.; Yuan, Z.; Zhao, Y.; Zhang, H.; Zhang, H.; Li, X. Porous Membranes in Secondary Battery Technologies. *Chem. Soc. Rev.* **2017**, *46* (8), 2199−2236.

(5) Castejon, P.; Habibi, K.; Saffar, A.; Ajji, A.; Martinez, A.; Arencon, D. Polypropylene-Based Porous Membranes: Influence of Polymer Composition, Extrusion Draw Ratio and Uniaxial Strain. *Polymers* **2018**, *10* (1), 33.

(6) Saffar, A.; Carreau, P. J.; Ajji, A.; Kamal, M. R. Influence of Stretching on the Performance of Polypropylene-Based Microporous Membranes. *Ind. Eng. Chem. Res.* **2014**, *53* (36), 14014−14021.

(7) Zhang, S. S. A Review on the Separators of Liquid Electrolyte Li-Ion Batteries. *J. Power Sources* **2007**, *164* (1), 351−364.

(8) Huang, X. Separator Technologies for Lithium-Ion Batteries. *J. Solid State Electrochem* **2011**, *15* (4), 649−662.

(9) Kim, J.-H.; Kim, J.-H.; Choi, E.-S.; Yu, H. K.; Kim, J. H.; Wu, Q.; Chun, S.-J.; Lee, S.-Y.; Lee, S.-Y. Colloidal Silica Nanoparticle-Assisted Structural Control of Cellulose Nanofiber Paper Separators for Lithium-Ion Batteries. *J. Power Sources* **2013**, *242*, 533−540.

(10) Man, C.; Jiang, P.; Wong, K.-w.; Zhao, Y.; Tang, C.; Fan, M.; Lau, W.-m.; Mei, J.; Li, S.; Liu, H.; Hui, D. Enhanced Wetting Properties of a

Polypropylene Separator for a Lithium-Ion Battery by Hyperthermal Hydrogen Induced Cross-Linking of Poly(Ethylene Oxide). *J. Mater. Chem. A* **2014**, *2* (30), 11980−11986.
(11) Ryou, M.-H.; Lee, Y. M.; Park, J.-K.; Choi, J. W. Mussel-Inspired Polydopamine-Treated Polyethylene Separators for High-Power Li-Ion Batteries. *Adv. Mater.* **2011**, *23* (27), 3066−3070.
(12) Kim, K. J.; Kim, J.-H.; Park, M.-S.; Kwon, H. K.; Kim, H.; Kim, Y.-J. Enhancement of Electrochemical and Thermal Properties of Polyethylene Separators Coated with Polyvinylidene Fluoride−Hexafluoropropylene Co-Polymer for Li-Ion Batteries. *J. Power Sources* **2012**, *198*, 298−302.
(13) Liu, Y.; Ma, H.; Hsiao, B. S.; Chu, B.; Tsou, A. H. Improvement of Meltdown Temperature of Lithium-Ion Battery Separator Using Electrospun Polyethersulfone Membranes. *Polymer* **2016**, *107*, 163−169.
(14) Shi, C.; Zhang, P.; Chen, L.; Yang, P.; Zhao, J. Effect of a Thin Ceramic-Coating Layer on Thermal and Electrochemical Properties of Polyethylene Separator for Lithium-Ion Batteries. *J. Power Sources* **2014**, *270*, 547−553.
(15) Shi, C.; Dai, J.; Li, C.; Shen, X.; Peng, L.; Zhang, P.; Wu, D.; Sun, D.; Zhao, J. A Modified Ceramic-Coating Separator with High-Temperature Stability for Lithium-Ion Battery. *Polymers* **2017**, *9* (12), 159.
(16) Wang, Z.; Xiang, H.; Wang, L.; Xia, R.; Nie, S.; Chen, C.; Wang, H. A Paper-Supported Inorganic Composite Separator for High-Safety Lithium-Ion Batteries. *J. Membr. Sci.* **2018**, *553*, 10−16.
(17) Yu, L.; Miao, J.; Jin, Y.; Lin, J. Y. S. A Comparative Study on Polypropylene Separators Coated with Different Inorganic Materials for Lithium-Ion Batteries. *Front. Chem. Sci. Eng.* **2017**, *11* (3), 346−352.
(18) Kim, J.-H.; Kim, J.-H.; Kim, J.-M.; Lee, Y.-G.; Lee, S.-Y. Superlattice Crystals−Mimic, Flexible/Functional Ceramic Membranes: Beyond Polymeric Battery Separators. *Adv. Energy Mater.* **2015**, *5* (24), 1500954.
(19) Lee, Y.; Lee, H.; Lee, T.; Ryou, M.-H.; Lee, Y. M. Synergistic Thermal Stabilization of Ceramic/Co-Polyimide Coated Polypropylene Separators for Lithium-Ion Batteries. *J. Power Sources* **2015**, *294*, 537−544.
(20) Xu, W.; Wang, Z.; Shi, L.; Ma, Y.; Yuan, S.; Sun, L.; Zhao, Y.; Zhang, M.; Zhu, J. Layer-by-Layer Deposition of Organic−Inorganic Hybrid Multilayer on Microporous Polyethylene Separator to Enhance the Electrochemical Performance of Lithium-Ion Battery. *ACS Appl. Mater. Interfaces* **2015**, *7* (37), 20678−20686.
(21) Dai, J.; Shi, C.; Li, C.; Shen, X.; Peng, L.; Wu, D.; Sun, D.; Zhang, P.; Zhao, J. A Rational Design of Separator with Substantially Enhanced Thermal Features for Lithium-Ion Batteries by the Polydopamine−Ceramic Composite Modification of Polyolefin Membranes. *Energy Environ. Sci.* **2016**, *9* (10), 3252−3261.
(22) Zhai, Y.; Wang, N.; Mao, X.; Si, Y.; Yu, J.; Al-Deyab, S. S.; El-Newehy, M.; Ding, B. Sandwich-Structured PVdF/PMIA/PVdF Nanofibrous Separators with Robust Mechanical Strength and Thermal Stability for Lithium Ion Batteries. *J. Mater. Chem. A* **2014**, *2* (35), 14511−14518.
(23) Hu, S.; Lin, S.; Tu, Y.; Hu, J.; Wu, Y.; Liu, G.; Li, F.; Yu, F.; Jiang, T. Novel Aramid Nanofiber-Coated Polypropylene Separators for Lithium Ion Batteries. *J. Mater. Chem. A* **2016**, *4* (9), 3513−3526.
(24) Wang, H.; Wang, T.; Yang, S.; Fan, L. Preparation of Thermal Stable Porous Polyimide Membranes by Phase Inversion Process for Lithium-Ion Battery. *Polymer* **2013**, *54* (23), 6339−6348.
(25) Zhang, H.; Lin, C.-E.; Zhou, M.-Y.; John, A. E.; Zhu, B.-K. High Thermal Resistance Polyimide Separators Prepared via Soluble Precusor and Non-Solvent Induced Phase Separation Process for Lithium Ion Batteries. *Electrochim. Acta* **2016**, *187*, 125−133.
(26) Li, D.; Shi, D.; Feng, K.; Li, X.; Zhang, H. Poly (Ether Ether Ketone) (PEEK) Porous Membranes with Super High Thermal Stability and High Rate Capability for Lithium-Ion Batteries. *J. Membr. Sci.* **2017**, *530*, 125−131.
(27) Li, J.; Zhong, Q.; Yao, Y.; Bi, S.; Zhou, T.; Guo, X.; Wu, M.; Feng, T.; Xiang, R. Electrochemical Performance and Thermal Stability of the Electrospun PTFE Nanofiber Separator for Lithium-Ion Batteries. *J. Appl. Polym. Sci.* **2018**, *135* (29), 46508.
(28) Liu, J.; Qin, J.; Mo, Y.; Wang, S.; Han, D.; Xiao, M.; Meng, Y. Dongmei Han, Min Xiao, and Yuezhong Meng. Polyphenylene Sulfide Separator for High Safety Lithium-Ion Batteries. *J. Electrochem. Soc.* **2019**, *166* (8), A1644−A1652.
(29) Liu, Z.; Jiang, W.; Kong, Q.; Zhang, C.; Han, P.; Wang, X.; Yao, J.; Cui, G. A Core@sheath Nanofibrous Separator for Lithium Ion Batteries Obtained by Coaxial Electrospinning. *Macromol. Mater. Eng.* **2013**, *298* (7), 806−813.
(30) Peabody, C.; Arnold, C. B. The Role of Mechanically Induced Separator Creep in Lithium-Ion Battery Capacity Fade. *J. Power Sources* **2011**, *196* (19), 8147−8153.
(31) Zhang, S. S.; Xu, K.; Jow, T. R. An Inorganic Composite Membrane as the Separator of Li-Ion Batteries. *J. Power Sources* **2005**, *140* (2), 361−364.
(32) l'Abee, R.; DaRosa, F.; Armstrong, M. J.; Hantel, M. M.; Mourzagh, D. High Temperature Stable Li-Ion Battery Separators Based on Polyetherimides with Improved Electrolyte Compatibility. *J. Power Sources* **2017**, *345*, 202−211.
(33) Takemura, D.; Aihara, S.; Hamano, K.; Kise, M.; Nishimura, T.; Urushibata, H.; Yoshiyasu, H. A Powder Particle Size Effect on Ceramic Powder Based Separator for Lithium Rechargeable Battery. *J. Power Sources* **2005**, *146* (1), 779−783.
(34) Zhang, Y.; Wang, Z.; Xiang, H.; Shi, P.; Wang, H. A Thin Inorganic Composite Separator for Lithium-Ion Batteries. *J. Membr. Sci.* **2016**, *509*, 19−26.
(35) Lagadec, M. F.; Zahn, R.; Wood, V. Characterization and Performance Evaluation of Lithium-Ion Battery Separators. *Nature Energy* **2019**, *4* (1), 16−25.
(36) Friesen, A.; Hildebrand, S.; Horsthemke, F.; Borner, M.; Klopsch, R.; Niehoff, P.; Schappacher, F. M.; Winter, M. Al2O3 coating on anode surface in lithium ion batteries: Impact on low temperature cycling and safety behavior. *J. Power Sources* **2017**, *363*, 70−77.
(37) Jung, Y.-C.; Kim, S.-K.; Kim, M.-S.; Lee, J.-H.; Han, M.-S.; Kim, D.-H.; Shin, W.-C.; Ue, M.; Kim, D.-W. Ceramic Separators Based on Li+-Conducting Inorganic Electrolyte for High-Performance Lithium-Ion Batteries with Enhanced Safety. *J. Power Sources* **2015**, *293*, 675−683.
(38) Sharma, G.; Jin, Y.; Lin, Y. S. Lithium Ion Batteries with Alumina Separator for Improved Safety. *J. Electrochem. Soc.* **2017**, *164* (6), A1184−A1191.
(39) Dai, M.; Shen, J.; Zhang, J.; Li, G. A Novel Separator Material Consisting of ZeoliticImidazolate Framework-4 (ZIF-4) and Its Electrochemical Performance for Lithium-Ions Battery. *J. Power Sources* **2017**, *369*, 27−34.
(40) Blake, A. J.; Kohlmeyer, R. R.; Hardin, J. O.; Carmona, E. A.; Maruyama, B.; Berrigan, J. D.; Huang, H.; Durstock, M. F. 3D Printable Ceramic-Polymer Electrolytes for Flexible High-Performance Li-Ion Batteries with Enhanced Thermal Stability. *Adv. Energy Mater.* **2017**, *7* (14), 1602920.
(41) Singh, N.; Galande, C.; Miranda, A.; Mathkar, A.; Gao, W.; Reddy, A. L. M.; Vlad, A.; Ajayan, P. M. Paintable Battery. *Sci. Rep* **2012**, *2* (1), 1−5.
(42) Huang, C.; Zhang, J.; Snaith, H. J.; Grant, P. S. Engineering the Membrane/Electrode Interface To Improve the Performance of Solid-State Supercapacitors. *ACS Appl. Mater. Interfaces* **2016**, *8* (32), 20756−20765.
(43) Huang, C.; Young, N.; Zhang, J.; Snaith, H.; Grant, P. A Two Layer Electrode Structure for Improved Li Ion Diffusion and Volumetric Capacity in Li Ion Batteries. *Nano Energy* **2016**, *31*, 11.
(44) Bu, J.; Leung, P.; Huang, C.; Lee, S. H.; Grant, P. S. Co-Spray Printing of LiFePO4 and PEO-Li1.5Al0.5Ge1.5(PO4)3 Hybrid Electrodes for All-Solid-State Li-Ion Battery Applications. *J. Mater. Chem. A* **2019**, *7* (32), 19094−19103.
(45) Cheng, C.; Drummond, R.; Duncan, S. R.; Grant, P. S. Combining Composition Graded Positive and Negative Electrodes for Higher Performance Li-Ion Batteries. *J. Power Sources* **2019**, 227376.

https://doi.org/10.1021/acsami.2c03828
ACS Appl. Mater. Interfaces 2022, 14, 34538−34551

(46) Lee, S. H.; Johnston, C.; Grant, P. S. Scalable, Large-Area Printing of Pore-Array Electrodes for Ultrahigh Power Electrochemical Energy Storage. *ACS Appl. Mater. Interfaces* **2019**, *11* (41), 37859−37866.
(47) Lee, S. Ho; Li, K.; Huang, C.; Evans, J. D.; Grant, P. S. Spray-Printed and Self-Assembled Honeycomb Electrodes of Silicon-Decorated Carbon Nanofibers for Li-Ion Batteries. *ACS Appl. Mater. Interfaces* **2019**, *11* (1), 603−612.
(48) Huang, X.; Hitt, J. Lithium Ion Battery Separators: Development and Performance Characterization of a Composite Membrane. *J. Membr. Sci.* **2013**, *425*−*426*, 163−168.
(49) Zhu, Y.; Xie, J.; Pei, A.; Liu, B.; Wu, Y.; Lin, D.; Li, J.; Wang, H.; Chen, H.; Xu, J.; Yang, A.; Wu, C.-L.; Wang, H.; Chen, W.; Cui, Y. Fast Lithium Growth and Short Circuit Induced by Localized-Temperature Hotspots in Lithium Batteries. *Nat. Commun.* **2019**, *10* (1), 1−7.
(50) Parsa, M.; Harmand, S.; Sefiane, K. Mechanisms of Pattern Formation from Dried Sessile Drops. *Adv. Colloid Interface Sci.* **2018**, *254*, 22−47.
(51) Love, C. T. Love. Thermomechanical Analysis and Durability of Commercial Micro-Porous Polymer Li-Ion Battery Separators. *J. Power Sources* **2011**, *196* (5), 2905−2912.
(52) Lagadec, M. F.; Ebner, M.; Zahn, R.; Wood, V. Communication—Technique for Visualization and Quantification of Lithium-Ion Battery Separator Microstructure. *J. Electrochem. Soc.* **2016**, *163* (6), A992−A994.
(53) Thommes, M.; Kaneko, K.; Neimark, A. V.; Olivier, J. P.; Rodriguez-Reinoso, F.; Rouquerol, J.; Sing, K. S.W. Physisorption of Gases, with Special Reference to the Evaluation of Surface Area and Pore Size Distribution (IUPAC Technical Report). *Pure Appl. Chem.* **2015**, *87* (9−10), 1051−1069.
(54) Ravikovitch, P. I.; Neimark, A. V. Experimental Confirmation of Different Mechanisms of Evaporation from Ink-Bottle Type Pores: Equilibrium, Pore Blocking, and Cavitation. *Langmuir* **2002**, *18* (25), 9830−9837.
(55) Wang, J.; Mei, X.; Huang, L.; Zheng, Q.; Qiao, Y.; Zang, K.; Mao, S.; Yang, R.; Zhang, Z.; Gao, Y.; Guo, Z.; Huang, Z.; Wang, Q. Synthesis of Layered Double Hydroxides/Graphene Oxide Nanocomposite as a Novel High-Temperature CO_2 Adsorbent. *J. Energy Chem.* **2015**, *24* (2), 127−137.
(56) Wu, S.; Shen, X.; Zhu, G.; Hu, Z.; Ji, Z.; Chen, K.; Yuan, A. Synthesis of Ternary Ag/ZnO/ZnFe2O4 Porous and Hollow Nanostructures with Enhanced Photocatalytic Activity. *Appl. Catal. B: Environmental* **2015**, DOI: 10.1016/j.apcatb.2015.11.035.
(57) Park, S.; Shin, D. O.; Lee, C. S.; Lee, Y.-G.; Kim, J. Y.; Kim, K. M.; Shin, K. Mesoporous Perforated Co 3 O 4 Nanoparticles with a Thin Carbon Layer for High Performance Li-Ion Battery Anodes. *Electrochim. Acta* **2018**, DOI: 10.1016/j.electacta.2018.01.092.
(58) McNeill, I. C.; Sadeghi, S. M. T. Thermal Stability and Degradation Mechanisms of Poly(Acrylic Acid) and Its Salts: Part 1—Poly(Acrylic Acid). *Polym. Degrad. Stab.* **1990**, *29* (2), 233−246.
(59) Dubinsky, S.; Grader, G. S.; Shter, G. E.; Silverstein, M. S. Thermal Degradation of Poly(Acrylic Acid) Containing Copper Nitrate. *Polym. Degrad. Stab.* **2004**, *86* (1), 171−178.
(60) Ruiz-Rubio, L.; Alvarez, V.; Lizundia, E.; Vilas, J. L.; Rodriguez, M.; Leon, L. M. Influence of α-Methyl Substitutions on Interpolymer Complexes Formation between Poly(Meth)Acrylic Acids and Poly(N-Isopropyl(Meth)Acrylamide)s. *Colloid Polym. Sci.* **2015**, *293* (5), 1447−1455.
(61) Greenberg, A. R.; Kamel, I.. Kinetics of Anhydride Formation in Poly(Acrylic Acid) and Its Effect on the Properties of a PAA-Alumina Composite. *Journal of Polymer Science: Polymer Chemistry Edition* **1977**, *15* (9), 2137−2149.
(62) De, D.; De, D. Processing and Material Characteristics of a Reclaimed Ground Rubber Tire Reinforced Styrene Butadiene Rubber. *Materials Sciences and Applications* **2011**, *02* (05), 486−495.
(63) Wefers, K. *Oxides and Hydroxides of Aluminum*; Alcoa Technical Paper No. 19, Revised. Aluminum Company of America, 1987.
(64) Jiang, F.; Yin, L.; Yu, Q.; Zhong, C.; Zhang, J. Bacterial Cellulose Nanofibrous Membrane as Thermal Stable Separator for Lithium-Ion Batteries. *J. Power Sources* **2015**, *279*, 21−27.
(65) Xie, Y.; Zou, H.; Xiang, H.; Xia, R.; Liang, D.; Shi, P.; Dai, S.; Wang, H. Enhancement on the Wettability of Lithium Battery Separator toward Nonaqueous Electrolytes. *J. Membr. Sci.* **2016**, *503*, 25−30.
(66) Yourey, J. E.; Bartlett, B. M. Electrochemical Deposition and Photoelectrochemistry of CuWO4, a Promising Photoanode for Water Oxidation. *J. Mater. Chem.* **2011**, *21* (21), 7651.
(67) Chu, Z.; Feng, X.; Liaw, B.; Li, Y.; Lu, L.; Li, J.; Han, X.; Ouyang, M. Xuebing Han, and Minggao Ouyang. Testing Lithium-Ion Battery with the Internal Reference Electrode: An Insight into the Blocking Effect. *J. Electrochem. Soc.* **2018**, *165* (14), A3240−A3248.
(68) Lee, S. H.; Huang, C.; Grant, P. S. Layer-by-Layer Printing of Multi-Layered Heterostructures Using Li4Ti5O12 and Si for High Power Li-Ion Storage. *Nano Energy* **2019**, *61*, 96−103.
(69) Leung, P.; Bu, J.; Quijano Velasco, P.; Roberts, M. R.; Grobert, N.; Grant, P. S. Single-Step Spray Printing of Symmetric All-Organic Solid-State Batteries Based on Porous Textile Dye Electrodes. *Adv. Energy Mater.* **2019**, *9* (39), 1901418.
(70) Ludwig, B.; Zheng, Z.; Shou, W.; Wang, Y.; Pan, H. Solvent-Free Manufacturing of Electrodes for Lithium-ion Batteries. *Sci. Rep.* **2016**, *6* (1), 23150.